J. Fluid Mech. (2010), *vol.* 644, *pp.* 337–357.
doi:10.1017/S0022112009992400

Onset of Küppers–Lortz-like dynamics in finite rotating thermal convection

A. RUBIO[1], J. M. LOPEZ[1]† AND F. MARQUES[2]

[1]Department of Mathematics and Statistics, Arizona State University, Tempe AZ 85287, USA

[2]Departament de Física Aplicada, Universitat Politècnica de Catalunya, Barcelona 08034, Spain

(Received 4 June 2009; revised 22 September 2009; accepted 22 September 2009)

The onset of thermal convection in a finite rotating cylinder is investigated using direct numerical simulations of the Navier–Stokes equations with the Boussinesq approximation in a regime in which spatio-temporal complexity is observed directly after onset. The system is examined in the non-physical limit of zero centrifugal force as well as with an experimentally realizable centrifugal force, leading to two different paths to Küppers–Lortz-like spatio-temporal chaos. In the idealized case, neglecting centrifugal force, the onset of convection occurs directly from a conduction state, resulting in square patterns with slow roll switching, followed at higher thermal driving by straight roll patterns with faster roll switching. The case with a centrifugal force typical of laboratory experiments exhibits target patterns near the theoretically predicted onset of convection, followed by a rotating wave that emerges via a Hopf bifurcation. A subsequent Hopf bifurcation leads to ratcheting states with sixfold symmetry near the axis. With increasing thermal driving, roll switching is observed within the ratcheting lattice before Küppers–Lortz-like spatio-temporal chaos is observed with the dissolution of the lattice at a slightly stronger thermal driving. For both cases, all of these states are observed within a 2 % variation in the thermal driving.

1. Introduction

Rotating convection has long been a paradigm problem in which to study the emergence of spatio-temporal chaos, as such states are observed to appear supercritically with the onset of convection when the fluid layer is rotating at a sufficiently fast angular velocity. These chaotic states found in laboratory and numerical experiments (e.g. see the reviews by Knobloch 1998; Bodenschatz, Pesch & Ahlers 2000) are associated with the theoretical predictions of Küppers & Lortz (1969) and Küppers (1970) who explored the linear stability of straight rolls in a horizontally infinite rotating layer with respect to other straight roll patterns oriented at different angles. They found that for rotation rates above a critical threshold, no steady-state roll patterns were stable, as they lose stability to another set of straight rolls oriented at an angle of about 59° to the first set. Laboratory experiments (conducted in finite containers) have shown complexity in both space and time in the guise of patches of re-orienting rolls immediately above the onset for rotation

† Email address for correspondence: lopez@math.la.asu.edu

rates above the critical rate predicted by Küppers & Lortz (1969), although the mechanism for the onset of spatio-temporal complexity observed in experiments is qualitatively different from that suggested from the infinite layer results (Bodenschatz *et al.* 1992; Hu *et al.* 1998). There has been a general expectation that a supercritical bifurcation from the spatially uniform conduction state leads directly to Küppers–Lortz-type spatio-temporal convective chaos and hence that it may be amenable to weakly nonlinear theory (Heikes & Busse 1980*a*,*b*; Niemela & Donnelly 1986; Zhong, Ecke & Steinberg 1991; Rodríguez *et al.* 1992; Tu & Cross 1992; Cross, Meiron & Tu 1994; Hu, Ecke & Ahlers 1997; Ponty, Passot & Sulem 1997; Hu *et al.* 1998; Cox & Matthews 2000; Bajaj, Ahlers & Pesch 2002; Becker & Ahlers 2006*a*,*b*; Jayaraman *et al.* 2006). While this form of spatio-temporal dynamics is inherently associated with the rotation of the system, its analysis has largely been restricted to considerations of the interplay between the Coriolis force and gravitational buoyancy, neglecting the effects of centrifugal accelerations.

It has long been understood that any rotating stratified fluid in a container must exhibit a centrifugally driven large-scale circulation (LSC) (Barcilon & Pedlosky 1967; Koschmieder 1967; Rossby 1969; Brummell, Hart & Lopez 2000). When the centrifugal acceleration is weak compared with that of gravity, the centrifugally driven LSC is negligible compared with the flow driven by gravitational buoyancy for thermal forcing only slightly beyond critical, and the effects of the centrifugal force are usually neglected in theoretical treatments and in interpretations of laboratory experiments. However, since the emergence of convection is supercritical, very near the onset the centrifugally driven LSC with small but finite amplitude is dominant in organizing the flow. As noted by Rossby (1969), '[w]hen the apparatus is rotated, a radial acceleration, which increases with radius, is established .... However, since this radial acceleration destroys the horizontal uniformity, which is a basic assumption in the Bénard convection problem, it is essential that its influence be minimized. Obviously the radial acceleration cannot be eliminated entirely'.

There have been previous studies of the impact of the centrifugal buoyancy on rotating convection, but the nonlinearity of the problem had restricted the scope of the investigations. Since the basic state is no longer the trivial conduction state, it needs to be determined from a nonlinear simulation of the governing equations. Substantial insight into the problem came from axisymmetric considerations, but the use of the fast rotation limit (to simplify the problem in the asymptotic regime) reduced the applicability of the results, in particular with regard to laboratory experiments (Homsy & Hudson 1969, 1971; Torrest & Hudson 1974; Hart 2000). Whereas most of those efforts were addressing the question of under what conditions the centrifugal buoyancy needs to be accounted for, Koschmieder (1993) took the following view: 'Actually of more interest is the question of what is the smallest acceleration ratio [gravitational to centrifugal] at which the centrifugal circulation in an unstably stratified rotating fluid layer can be neglected'. In this paper, we address a different issue; we wish to gain a deeper understanding of the onset of thermal convection in an enclosed rotating cylinder, particularly in parameter regimes typically accessed experimentally, where Küppers–Lortz dynamics are observed near the onset and the ratio of centrifugal acceleration to gravitational acceleration is small and hence the centrifugal buoyancy effects have typically been neglected.

Recently, there has been an interest in studying the effects of the centrifugal force with an emphasis on reconciling the results from reduced models with laboratory observations and numerical simulations of the Navier–Stokes–Boussinesq equations (Becker *et al.* 2006), although it has been noted that incorporating the

centrifugal force into a reduced partial differential equations model framework (e.g. the Swift–Hohenberg and Ginzburg–Landau models) is difficult if not impossible because of the fact that the additional term makes the Navier–Stokes equations inhomogeneous (Scheel 2007).

Our earlier studies have shown that even a relatively weak centrifugal force can have a substantial impact on the dynamics of axisymmetric rotating convection, where we have restricted the simulations to be axisymmetric (Lopez, Rubio & Marques 2006*b*). However, the onset of three-dimensional instabilities occurs at lower parameter values, and so those results do not address the onset of complicated dynamics in the system. More recently, Lopez & Marques (2009) showed that for cylinders of radius-to-height aspect ratios of order one, the dynamics are governed by a complicated tangle of codimension-two bifurcation points and that the onset of three-dimensional flow is substantially simplified as the relative strength of the centrifugal buoyancy is increased. However, the extensive Küppers–Lortz-like dynamics were not evident in such low-aspect-ratio cylinders. In this paper, we address these issues in cylinders of aspect ratios of order 10, where Küppers–Lortz dynamics near the onset are prevalent for the rotation rate considered.

In § 2, the governing equations and the numerical techniques to solve them are discussed. Section 3 contains four subsections detailing the linear stability analysis and nonlinear saturation of rotating convection, both neglecting and accounting for the centrifugal force. A discussion of the evidence for the centrifugally driven LSC in existing laboratory studies is presented in § 4, followed by the implications of our numerical study, including a discussion of the role played by the spectral gaps in pattern formation, in § 5.

2. Governing equations and numerical technique

Consider the flow in a circular cylinder, with no-slip boundary conditions, of radius r_0 and depth d, rotating with an angular frequency ω. The endwalls are maintained at constant temperatures, namely $T_0 - \Delta T/2$ at the top and $T_0 + \Delta T/2$ at the bottom, with an insulating sidewall. The Boussinesq approximation is implemented, treating all fluid properties as constant except for a linear variation of density with temperature in the gravitational and centrifugal buoyancy terms. The system is non-dimensionalized using d as the length scale, d^2/ν as the time scale (ν is the kinematic viscosity), $\nu^2\rho_0/d^2$ as the pressure scale (ρ_0 is the density at mean temperature T_0) and ΔT (the difference between the top and bottom temperatures) as the temperature scale. In a frame of reference rotating at rate ω, the non-dimensional governing equations are

$$(\partial_t + \boldsymbol{u}\cdot\nabla)\boldsymbol{u} = -\nabla p + \nabla^2\boldsymbol{u} + \frac{Ra}{\sigma}\Theta\boldsymbol{z} + 2\Omega\boldsymbol{u}\times\boldsymbol{z} - \frac{RaFr}{\sigma\gamma}(\Theta - z)\boldsymbol{r}, \tag{2.1}$$

$$(\partial_t + \boldsymbol{u}\cdot\nabla)\Theta = w + \sigma^{-1}\nabla^2\Theta, \quad \nabla\cdot\boldsymbol{u} = 0, \tag{2.2}$$

where $\boldsymbol{u} = (u, v, w)$ is the velocity in cylindrical coordinates (r, θ, z); p is the dynamic pressure; $\boldsymbol{r}$ is the radial unit vector in the r-direction; $\boldsymbol{z}$ is the vertical unit vector in the z-direction; and Θ is the temperature deviation with respect to the conductive linear temperature profile. The relationship between Θ and the non-dimensional temperature T is given by

$$T = T_0/\Delta T - z + \Theta, \tag{2.3}$$

where $T_0/\Delta T - z$ is the conductive temperature profile.

There are five independent non-dimensional parameters:

$$\begin{array}{ll} \text{Rayleigh number} & Ra = \alpha g d^3 \Delta T/\kappa\nu, \\ \text{Coriolis number} & \Omega = \omega d^2/\nu, \\ \text{Prandtl number} & \sigma = \nu/\kappa, \\ \text{aspect ratio} & \gamma = r_0/d, \\ \text{Froude number} & Fr = \omega^2 r_0/g, \end{array}$$

where α is the coefficient of volume expansion, κ the thermal diffusivity and g the acceleration because of gravity. The boundary conditions (in a frame of reference rotating at rate ω) are as follows:

$$r = \gamma, \quad \Theta_r = u = v = w = 0;$$
$$z = \pm 0.5, \quad \Theta = 0, \quad u = v = w = 0.$$

The governing equations are solved using the second-order time-splitting of Hughes & Randriamampianina (1998), combined with a pseudo-spectral method for the spatial discretization, utilizing a Galerkin–Fourier expansion in the azimuthal coordinate θ and the Chebyshev collocation in r and z. Following Orszag & Patera (1983), we have used the combinations $u_+ = u + \mathrm{i}v$ and $u_- = u - \mathrm{i}v$ in order to decouple the linear diffusion terms in the momentum equations. For each Fourier mode, the resulting Helmholtz equations for Θ, w, u_+ and u_- have been solved using a diagonalization technique in the two coordinates r and z. The coordinate singularity at the axis ($r = 0$) is treated following the prescription in Fornberg (1998), which guarantees the regularity conditions at the origin needed to solve the Helmholtz equations (Mercader, Net & Falqués 1991).

The code has been validated on a number of convection problems in rotating cylinders (Lopez, Rubio & Marques 2006*b*; Lopez *et al.* 2007; Marques *et al.* 2007; Rubio, Lopez & Marques 2008, 2009; Lopez & Marques 2009), establishing resolution requirements over a wide range of parameters. For the cases considered in this paper, $n_r = 64$ and $n_z = 24$ Chebyshev modes in r and z, respectively, were employed except where noted otherwise. For cases in which the solution is non-axisymmetric, $n_\theta = 184$ Fourier modes in θ were used. The time discretization used $\delta t \leqslant 0.0225$ viscous time units. For the majority of the simulations, the Coriolis number $\Omega = 19.7$, the Prandtl number $\sigma = 4.5$ and the aspect ratio $\gamma = 11.8$ are fixed to correspond to those in relevant experiments (Thompson, Bajaj & Ahlers 2002), and we consider variations in Ra for $Fr = 0$ and 8.82×10^{-3} to illustrate the differences between the route to complexity in the idealized case neglecting the centrifugal buoyancy and that seen in laboratory experiments with small but finite centrifugal acceleration. Even for $0 < Fr \ll 1$, the centrifugal buoyancy may not be neglected *a priori* compared with gravitational buoyancy, since the two act in orthogonal directions (r and z, respectively).

The linear stability analysis, discussed in §§ 3.1, 3.3 and 4, was performed via direct numerical stability analysis. First, a steady axisymmetric basic state is computed at some point in parameter space, and its stability is determined by introducing small random perturbations into all azimuthal Fourier modes. For sufficiently small perturbations, the nonlinear couplings between Fourier modes are negligible (below the round-off numerical noise), and the growth rates (the real parts of the eigenvalues) and structure of the eigenfunctions corresponding to the fastest growing perturbation at each Fourier mode emerge from time evolution. This is tantamount to a matrix-free power method in which the actions of the Jacobian matrices for the perturbations

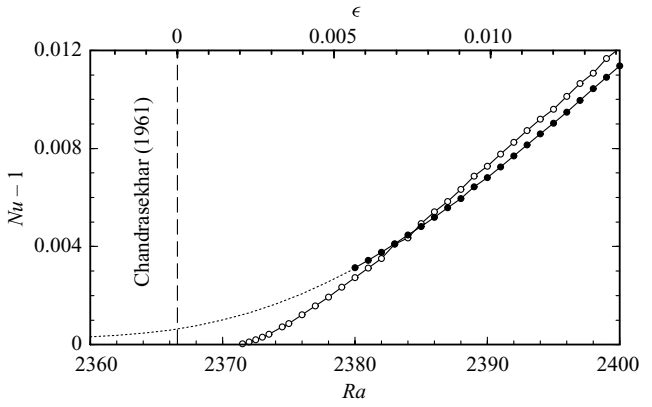

FIGURE 1. Average Nusselt number variation with Ra (and ϵ) for $Fr = 0$ (open circles) and $Fr = 8.82 \times 10^{-3}$ (filled circles), for fixed $\Omega = 19.7$, $\sigma = 4.5$ and $\gamma = 11.8$. The dotted curve shows $Nu - 1$ for the axisymmetric base state with $Fr = 8.82 \times 10^{-3}$ when it is stable to three-dimensional perturbations. The dashed vertical line shows the estimate of Chandrasekhar (1961) for the onset of convection for $\Omega = 19.7$ in an unbounded layer.

are given by time integration of the Navier–Stokes–Boussinesq equations with the aforementioned initial conditions. Using this method, a direct comparison between the stability analysis of the $Fr = 0$ case, whose basic state is the trivial conduction state, and the $Fr = 8.82 \times 10^{-3}$ case, whose non-trivial basic state must be computed in the axisymmetric subspace, can be made. Furthermore, it is very efficient, as the exponential growth or decay of the perturbations is established in a relatively short evolution time (there is no need to evolve the disturbances until they saturate nonlinearly), and by using estimates of the real parts of the eigenvalues from these growth/decay rates for a small number of points in parameter space in the neighbourhood of a bifurcation point, linear interpolation of the rates to zero provides a very good estimate of the bifurcation point. Moreover, the same technique is used to study the linear stability of three-dimensional rotating waves that have been computed in appropriate Fourier subspaces.

3. Results

The heat transfer properties of a solution are characterized by the Nusselt number, the ratio between the heat transfer of the solution considered and the heat transfer of the conductive state, both through the top lid. It is given by

$$Nu = -\frac{1}{\pi\gamma^2} \int_{r=0}^{r=\gamma} \int_{\theta=0}^{\theta=2\pi} \frac{\partial T}{\partial z}\bigg|_{z=0.5} r \, \mathrm{d}r \, \mathrm{d}\theta. \tag{3.1}$$

Figure 1 shows the time-averaged Nusselt number as a function of Ra for fully saturated simulations at $\Omega = 19.7$, $\gamma = 11.8$ and $\sigma = 4.5$, both neglecting and incorporating the centrifugal force, $Fr = 0$ and $Fr = 8.82 \times 10^{-3}$, respectively. When the centrifugal force is neglected, the average Nusselt number grows supercritically from unity. With the centrifugal force accounted for, the solution is axisymmetric with a Nusselt number greater than unity for $0 < Ra < 2380$. These axisymmetric patterns, described in § 3.3, grow smoothly in amplitude near the critical Ra given by Chandrasekhar (1961), resulting in a rounding of the Nusselt number curve. At $Ra = 2380$, this axisymmetric state loses stability to three-dimensional perturbations.

3.1. $Fr = 0$ linear stability analysis

The linear stability analysis of the conduction state (neglecting the centrifugal buoyancy) was first performed, using a complete basis for the perturbations and allowing for Hopf bifurcations, by Goldstein *et al.* (1993), who showed that there are two types of convective modes, namely the wall modes consisting of a uniformly precessing wave made up of pairs of hot and cold plumes localized radially near the sidewall and the bulk modes consisting of convective motions in the interior of the cylinder. When the cylinder is rotating sufficiently fast, wall modes are the first modes to bifurcate from the conduction state as the temperature across the cylinder is increased, while the bulk modes are the primary bifurcation modes for slower rotation speeds at which Küppers–Lortz dynamics are observed near the onset in experiments. It is this regime in which the bulk modes are the primary convective instability that we focus on in this paper. Goldstein *et al.* (1993) observed that the bulk mode eigenfunctions are localized about the rotation axis and that eigenfunctions with even azimuthal wavenumbers are invariant to $R_\pi \cdot K$, whereas those with odd azimuthal wavenumbers are invariant to R_π. The actions of these symmetries on the velocity and temperature are

$$R_\pi(u, v, w, \Theta)(r, \theta, z, t) = (u, v, w, \Theta)(r, \theta + \pi, z, t), \tag{3.2}$$

$$K(u, v, w, \Theta)(r, \theta, z, t) = (u, v, -w, -\Theta)(r, \theta, -z, t). \tag{3.3}$$

Goldstein *et al.* (1993) also found that small variations in the parameters (Ra, Ω, σ and γ) change which bulk mode is first to bifurcate from the conduction state, and so with small adjustments in the parameters it is relatively easy to find high-codimension points at which a number of different bulk modes bifurcate simultaneously. The question naturally arises as to how do these high-codimension bifurcations affect the nonlinear dynamics near the onset. Even though this behaviour occurs very near the onset, because of mode interactions it is highly nonlinear, and we shall see that it is not readily amenable to weakly nonlinear treatments.

Figure 2(a) shows the marginal stability curves for Fourier modes with azimuthal wavenumbers $m \in [0, 10]$. The complicated interweaving of the curves is hidden by their proximity, and all 11 curves appear essentially as a single thick line. In order to disentangle the curves, the same data is re-plotted in figure 2(b) in terms of $\epsilon = (Ra - Ra_c(\Omega))/Ra_c(\Omega)$, where $Ra_c(\Omega)$ is the critical Ra at which the conduction state loses stability for a laterally infinite rotating fluid layer (Chandrasekhar 1961). We also find that for a given Ω, a number of modes of one parity (m odd or even) bifurcate from the conduction state at lower ϵ than any mode of the other parity does and that which parity is first to bifurcate varies with Ω.

Figure 3 shows the marginal stability curves for Fourier modes with $m \in [0, 34]$ and $\Omega = 19.7$, $\sigma = 4.5$, $\gamma = 11.8$ and $Fr = 0$. For these parameters, our linear stability analysis of the $Fr = 0$ case shows that the $m = 5$ perturbation is the first to bifurcate at $Ra \approx 2371.2$ as Ra is increased, followed rapidly by a number of other odd modes and then by a set of even modes. The first 10 modes bifurcate from the conduction state by $Ra \approx 2371.7$, a variation of about 0.02 % in Ra.

Figure 4 shows the structure of the first four eigenmodes to bifurcate from the conduction state with increasing Ra. All four eigenmodes precess slowly (the values of their precession rates $\partial\theta/\partial t$ are -1.67×10^{-5} for $m = 5$, -9.98×10^{-6} for $m = 3$, -2.69×10^{-5} for $m = 7$ and -6.90×10^{-6} for $m = 1$, with the negative sign indicating that the precession is retrograde) and closely resemble the bulk modes found in Goldstein *et al.* (1993), with the convection concentrated about the axis,

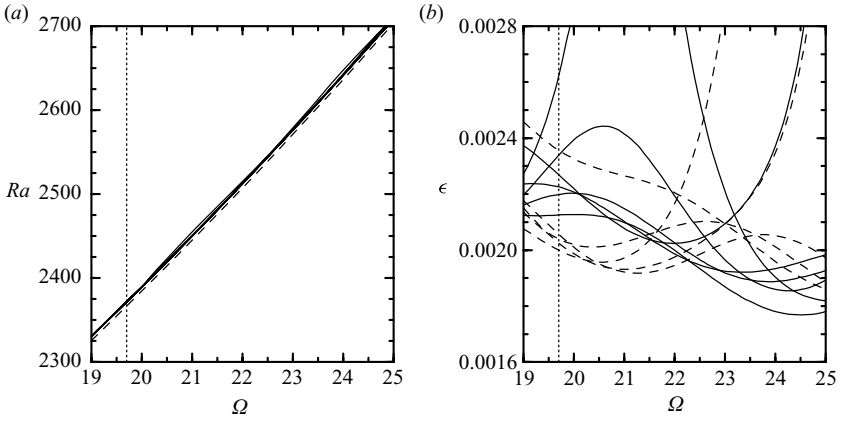

FIGURE 2. (*a*) Marginal stability curves (solid lines) for the eigenvectors corresponding to Fourier modes 0–10 of the linear stability analysis of rotating convection with $\sigma = 4.5$, $\gamma = 11.8$ and $Fr = 0$. A dotted vertical line indicates $\Omega = 19.7$, and a dashed line gives Chandrasekhar's estimate for the onset of convection in an infinite layer. (*b*) The same data as in (*a*) given in terms of $\epsilon = (Ra - Ra_c(\Omega))/Ra_c(\Omega)$, where $Ra_c(\Omega)$ is given by Chandrasekhar's estimate for the onset of convection. Even (odd) modes are shown as the solid (dashed) lines. The dotted vertical line is at $\Omega = 19.7$.

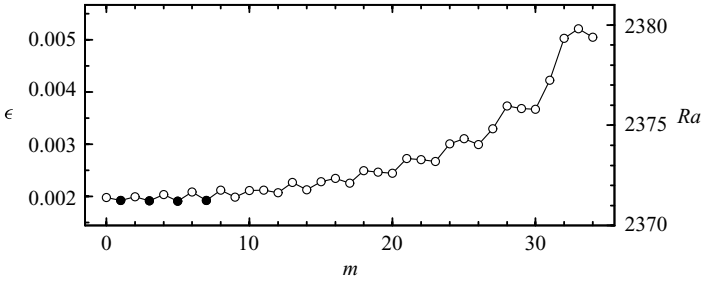

FIGURE 3. Critical thermal driving required for linear stability for eigenvectors corresponding to Fourier modes 0–34 at $\Omega = 19.7$ for $\sigma = 4.5$, $\gamma = 11.8$ and $Fr = 0$. The first four modes to bifurcate from the conduction state, in order, are $m = 5$, 3, 7 and 1 and are shown as filled circles.

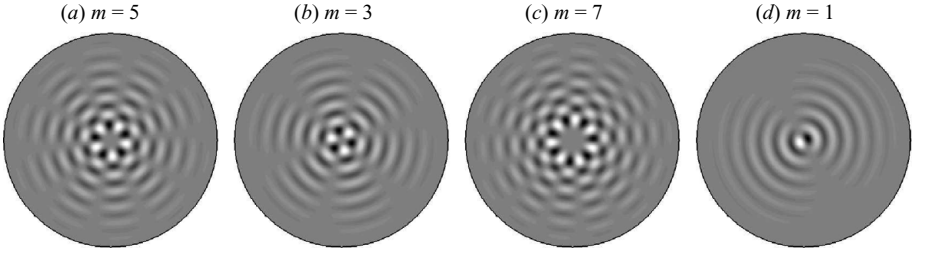

FIGURE 4. Snapshots of the first four eigenmodes to bifurcate from the conduction state as *Ra* is increased from 2371.2 to 2371.7, for $\Omega = 19.7$, $\sigma = 4.5$, $\gamma = 11.8$ and $Fr = 0$; their azimuthal wavenumbers are indicated.

diminishing rapidly with increasing radius. When these are evolved nonlinearly, the saturated solutions, whether computed in the full three-dimensional space or in a subspace corresponding to the representative Fourier mode of the perturbation, are quite different in their spatial and temporal structure from the small-amplitude perturbations of the linear stability analysis. Although the spectrum is discrete because of the finite confined geometry of the problem, the very small gaps in the spectrum make the application of weakly nonlinear dynamical systems approaches problematic. Since there are several distinct modes with very similar growth rates near the onset, one cannot *a priori* assume that the mode which first bifurcates will saturate nonlinearly without influence from nearby decaying modes. The whole concept of a low-dimensional centre manifold describing the weakly nonlinear dynamics near the onset becomes questionable because of the tight spectral gaps. With several near-critical modes, in principle, a high-dimensional centre manifold theory could be developed. When there are only two modes that are near critical, codimension-two dynamics have been successfully described and compared with experiments and fully nonlinear simulations in a number of fluid problems (e.g. Barkley, Tuckerman & Golubitsky 2000; Marques, Lopez & Shen 2002; Lewis & Nagata 2003; Lopez, Cui & Lim 2006*a*; Avila *et al.* 2008), and there are examples of codimension-three double Hopf bifurcations as well (Marques, Gelfgat & Lopez 2003), but with several such modes, the centre manifold description becomes unwieldly and impractical.

3.2. $Fr = 0$ *secondary instabilities*

When solutions at $\Omega = 19.7$, $\sigma = 4.5$, $\gamma = 11.8$ and $Fr = 0$ with Ra just above the value required for linear instability of the conduction state are allowed to saturate, exceedingly long transient times are encountered. As noted earlier, these patterns emerge supercritically from the conduction state. Snapshots of the nonlinearly saturated temperature perturbation Θ at $Ra = 2372$, 2373 and 2374 are shown in figures 5(*a*)–5(*c*), respectively. These solutions were time integrated to over 158 000 viscous times, corresponding to over 22 days in equivalent laboratory experiments. All these solutions are very different from the pure eigenmodes shown in figure 4. At $Ra = 2372$, a square lattice pattern centred and localized about the axis of rotation slowly precesses in the retrograde direction, exhibiting a barely noticeable degree of roll switching (supplementary movie 1 available at journals.cambridge.org/flm shows this evolution). It is difficult to say whether this solution has evolved beyond its initial transient, and determining the characteristics of this potentially quasi-periodic state would require a time integration well beyond the 158 000 viscous times already computed. We also note that a Fourier decomposition of this state shows that it has significant power in at least six Fourier modes $m \in [0, 91]$, as can be seen in figure 6(*a*) which shows the L2-norm of the kinetic energy associated with each Fourier mode of the saturated solutions as shown in figures 5(*a*)–5(*c*), where the L2-norm of a scalar function f is given by

$$\| f \|_2 = \left[\int_{-1/2}^{1/2} \int_0^{2\pi} \int_0^{\gamma} f^2(r, \theta, z)\, r \, \mathrm{d}r \, \mathrm{d}\theta \, \mathrm{d}z \right]^{1/2}. \tag{3.4}$$

At slightly higher $Ra = 2373$, the square lattice fills the fluid layer to a larger radius, and roll switching within the confines of the square lattice is clearly seen in supplementary movie 2. By $Ra = 2374$, the pattern fills the entire cell, and a seemingly quasi-periodic roll-switching state is observed (see supplementary movie 3). The growing extent of the square lattice for $Ra = 2373$ and 2374 is necessarily accompanied by an increase in amplitude of the higher Fourier modes required to

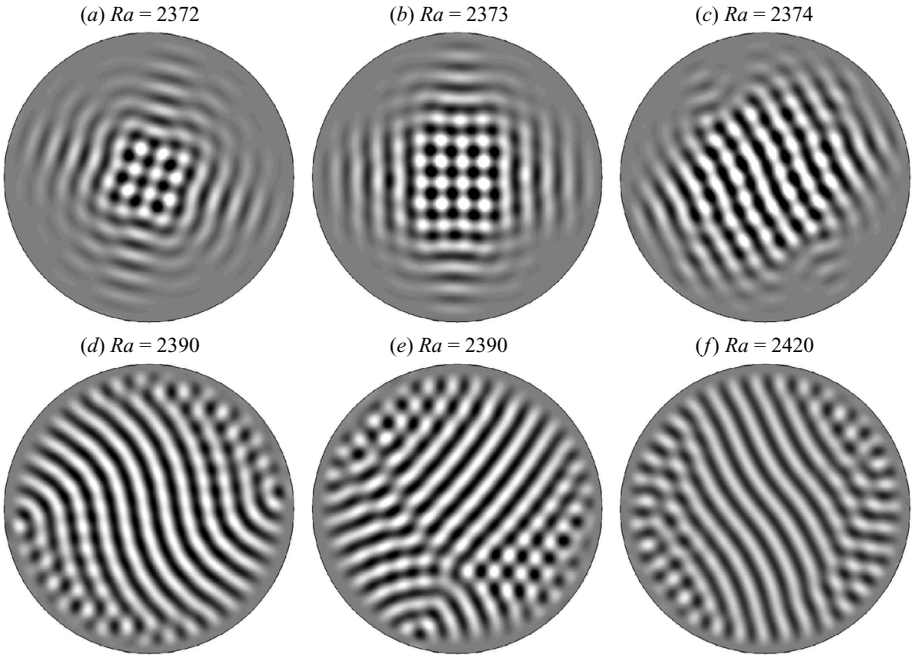

FIGURE 5. Snapshots of the temperature perturbation Θ at mid-height $z=0$ for $\Omega=19.7$, $\sigma=4.5$, $\gamma=11.8$, $Fr=0$ and indicated the Ra, with the colour levels of $\Theta\in[-5\epsilon, 5\epsilon]$ (black to white).

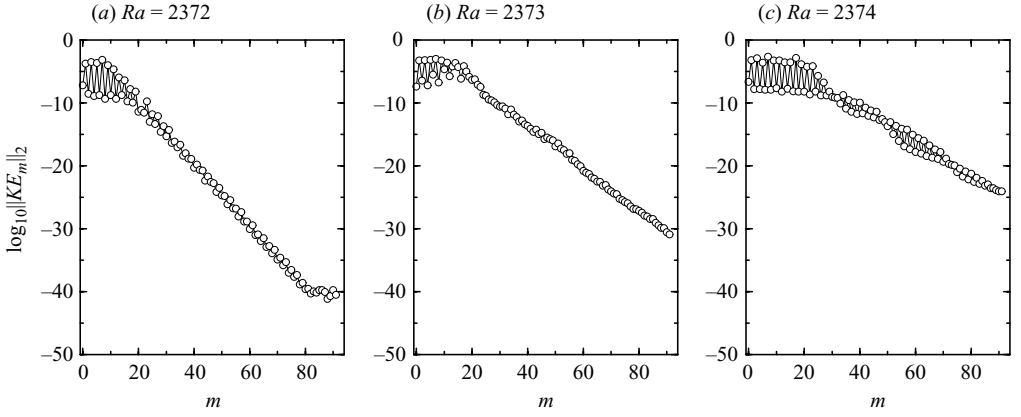

FIGURE 6. The L2-norm of the time-averaged kinetic energy associated with Fourier modes $m\in[0, 91]$ for simulations with $\Omega=19.7$, $\sigma=4.5$, $\gamma=11.8$, $Fr=0$ and Ra as indicated. Time-averaging was done over 60 000 viscous times for each solution.

resolve the square pattern at increasing radius, as can be seen in figures 6(*b*) and 6(*c*). At higher $Ra\in[2386, 2392]$, S-shaped roll patterns slowly precess for long times before more complicated behaviour in space and time sets in. This can be seen in the $Ra=2390$ time series shown in figure 7, where the roll pattern shown in figure 5(*d*) persisted for over 25 000 viscous times before its R_π-rotational symmetry was lost, resulting in states such as those in figure 5(*e*) with lines of defects gliding through the layer. Solutions at higher Ra exhibited global roll switching early in their time

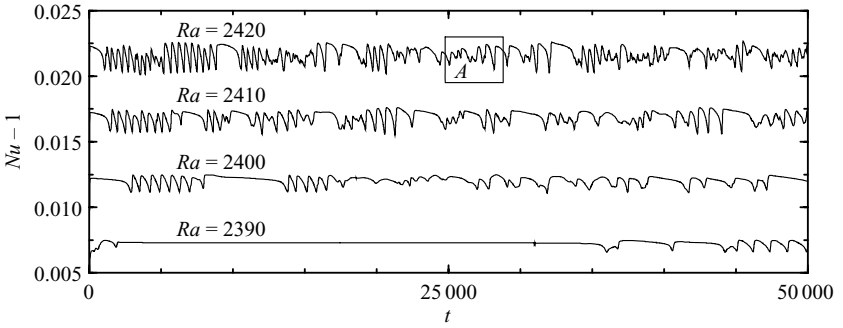

FIGURE 7. Time series of $Nu - 1$ at $Fr = 0$, $\Omega = 19.7$, $\sigma = 4.5$ and $\gamma = 11.8$, for Ra as indicated.

integrations, but all of them took on a more complicated temporal structure at later times as indicated by the $Ra = 2400$, 2410 and 2420 time series shown in figure 7. For both types of patterns, with either long stretches of quasi-steady behaviour or global roll switching, the onset of complex time behaviour is associated with a breaking of the R_π symmetry with lines of defects propagating relatively quickly across the cylinder in arbitrary directions.

Qualitative features of patterns such as those in figure 5(f), including defects originating at the sidewall and gliding through the fluid layer leading to patches of re-orienting rolls, have been reported in simulations of the Swift–Hohenberg equations in finite cylinders (Fantz *et al.* 1992). However, we are not aware of any report of the localized square patterns shown in figures 5(a) and 5(b) from simulations of reduced-equation models of rotating convection. Localized square patterns in rotating convection have been observed experimentally (Bajaj *et al.* 1998), but they have presented something of an enigma (Ahlers 2006) when trying to reconcile them with theory based on the assumption of horizontal periodicity. Theoretical treatments of square periodic lattices have shown them to be unstable, and yet laboratory experiments and numerical simulations of the Navier–Stokes–Boussinesq equations in confined rotating cylinders (neglecting the centrifugal buoyancy) have found states in which localized square patterns in the interior coexist with wall-localized plumes near the onset of bulk convection (Bajaj *et al.* 1998; Sánchez-Álvarez *et al.* 2005; Marques & Lopez 2008). However, localized square patterns without the prior presence of wall-localized plumes had not been previously reported in either laboratory experiments or numerical simulations. Of course, it is not clear whether there is any correspondence between the square tessellations in horizontally periodic problems and the patterns with locally fourfold symmetry found in laterally confined rotating convection. In our opinion, the two patterns are unrelated. The square patterns localized about the axis near the onset appear to be a nonlinear combination of the first several Fourier eigenmodes to bifurcate from the conduction state (the first four eigenmodes are shown in figure 4).

3.3. $Fr = 0.00882$ *linear stability analysis*

When the centrifugal force is not neglected, any non-zero Ra will result in an LSC in the fluid layer. However, for Fr small and Ra sufficiently above the value required for three-dimensional convection, this fluid motion is quite weak compared with the gravitational buoyancy-driven flow and often can be ignored. In theoretical models of rotating convection in infinite or periodic layers, the centrifugal buoyancy must be ignored, as it varies with the radial distance from the axis of rotation,

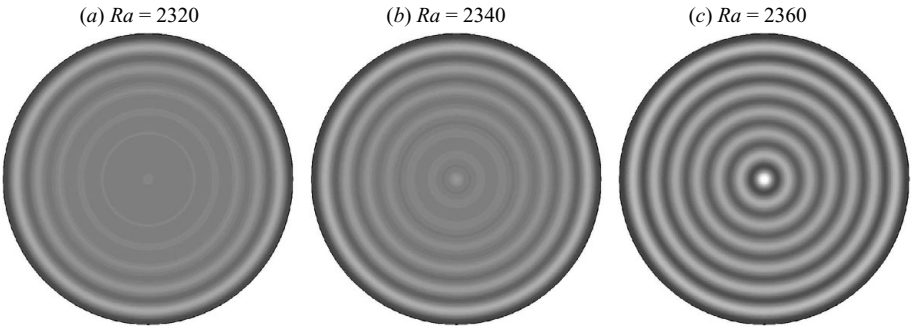

FIGURE 8. Temperature perturbation Θ at $z = 0$ for $\Omega = 19.7$, $\sigma = 4.5$, $\gamma = 11.8$, $Fr = 8.82 \times 10^{-3}$ and Ra as indicated, with color levels of $\Theta \in [-0.02, 0.02]$ (black to white).

violating the underlying assumptions of either horizontal translation invariance or periodicity; the location of the axis of rotation becomes distinguished and the centrifugal buoyancy becomes unbounded at large distances from the rotation axis. Numerical simulations neglecting the centrifugal force can agree quite well with laboratory experiments provided that the parameter regime explored is sufficiently beyond the onset of gravitational buoyancy-driven convection, depending on the ratio of centrifugal to gravitational accelerations. However, the finite-amplitude centrifugally driven LSC is necessarily the dominant flow very near the supercritical onset of gravitational buoyancy-driven convection. For $\Omega = 19.7$, $\sigma = 4.5$, $\gamma = 11.8$ and $Fr = 8.82 \times 10^{-3}$ (corresponding to the actual centrifugal force observed in similar laboratory experiments) this LSC is a target pattern that varies with parameters. Some examples are shown in figure 8. For small Ra, circular concentric rolls form at the periphery of the cylinder, strengthening and developing new rolls into the interior with increasing Ra, until near the onset of three-dimensional convection, where a target pattern fills the entire cylinder. The same development of the centrifugally driven LSC has been reported by Daniels (1980) from consideration of a simplified rotating convection problem with stress-free boundary conditions and restricted to steady axisymmetric flow using a perturbation analysis, as well as in the laboratory experiments of Koschmieder (1967, 1993).

For $Ra \in [2370, 2394]$, target patterns were computed in the axisymmetric subspace, and then their stability was determined by subjecting them to random perturbations in Θ with the L2-norm of order 10^{-10} across all Fourier modes. The linear stability analysis consisted of monitoring the exponential growth and decay of the amplitude of the perturbations associated with each Fourier mode. While the perturbations have the L2-norm of order 10^{-10}, the nonlinear coupling between them is of the order of 10^{-20}, ensuring that the nonlinear time evolution behaves as a direct linear stability analysis plus an error 10 orders of magnitude smaller than any of the relevant quantities. Time integration is tantamount to a generalization of the power method for finding eigenvalues with largest positive real part. After temporal evolution of a few viscous adjustment times, we find that for each Fourier mode the eigenfunction associated with the eigenvalue with the largest real part clearly emerges. A typical time series resulting from this process is shown in the first few thousand viscous times of figure 9(a), which shows the linear growth and decay of perturbations associated with Fourier modes $m \in [1, 92]$ followed by the nonlinear saturation of an $m = 23$ rotating wave (described in detail in the following section). The results of the linear stability analysis are shown in figures 10 and 11, consisting of the critical Ra values for $\Omega = 19.7$, $\sigma = 4.5$, $\gamma = 11.8$ and $Fr = 8.82 \times 10^{-3}$ and the eigenfunctions

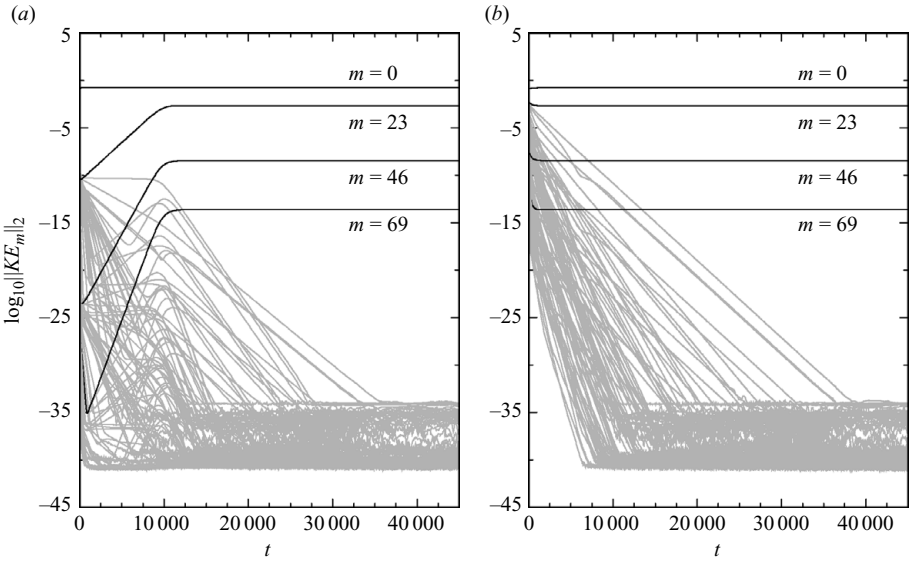

FIGURE 9. Time series of the L2-norm of the kinetic energy associated with each Fourier mode for simulations with $Ra = 2380$, $\Omega = 19.7$, $\sigma = 4.5$, $\gamma = 11.8$ and $Fr = 8.82 \times 10^{-3}$. (*a*) Saturation from below; the initial condition was an axisymmetric target pattern with a random perturbation of order 10^{-10} across all Fourier modes. (*b*) Decay from above; the initial condition was a fully developed solution with $Ra = 2400$ as shown in figure 13(*c*). In both cases the modal energies with $m = 0$, 23, 43 and 69 are shown as black lines, and all other modal energies are shown as grey lines.

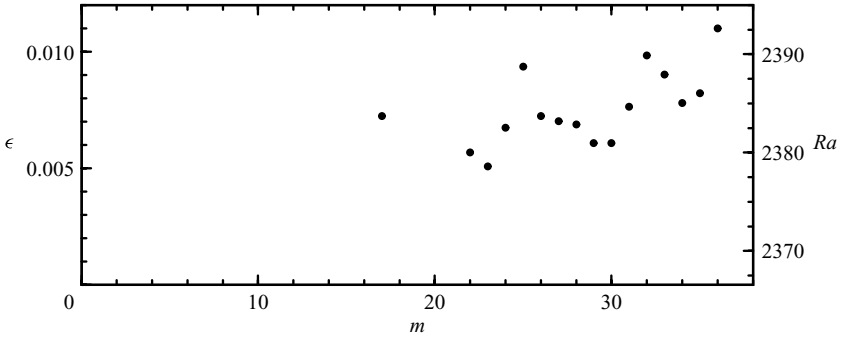

FIGURE 10. Critical Ra for disturbances with azimuthal wavenumber m at $\Omega = 19.7$, $\sigma = 4.5$, $\gamma = 11.8$ and $Fr = 8.82 \times 10^{-3}$.

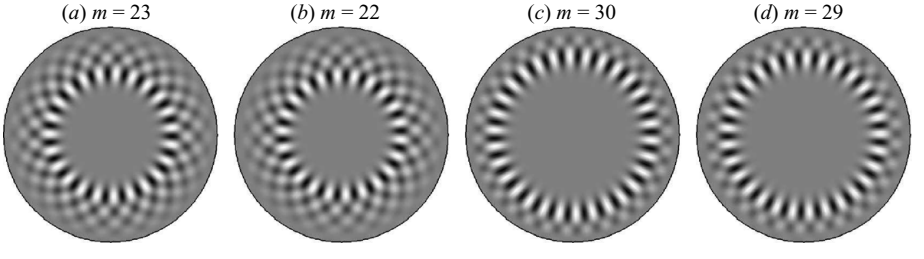

FIGURE 11. Snapshots of the four eigenmodes with fastest growth rate to bifurcate from the axisymmetric basic state at $Ra = 2380$, $\Omega = 19.7$, $\sigma = 4.5$, $\gamma = 11.8$ and $Fr = 8.82 \times 10^{-3}$.

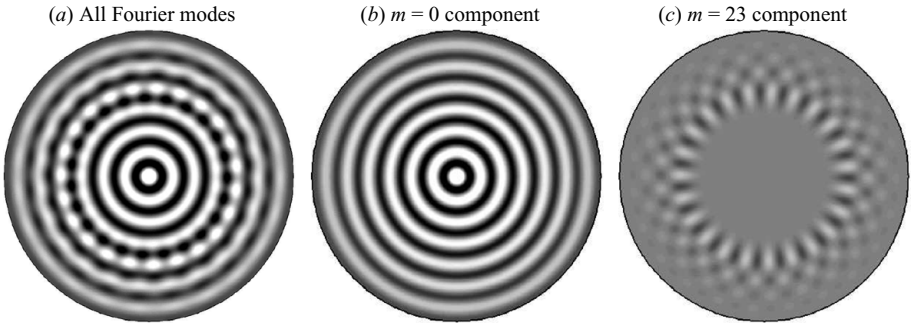

FIGURE 12. Temperature perturbation Θ at $z=0$ for $Ra=2380$, $\Omega=19.7$, $\sigma=4.5$, $\gamma=11.8$ and $Fr=8.82\times10^{-3}$; (*a*) shows the complete solution; (*b*) shows its axisymmetric component; and (*c*) shows its $m=23$ component, with color levels of $\Theta\in[-5\epsilon, 5\epsilon]$ (black to white).

corresponding to the first four non-axisymmetric perturbations to bifurcate from the basic state as Ra is increased; their precession rates, $\partial\theta/\partial t$, are 2.17×10^{-5} for $m=23$, -2.51×10^{-6} for $m=22$, 1.26×10^{-5} for $m=30$ and -1.33×10^{-5} for $m=29$, with the sign indicating whether the precession is retrograde (negative) or prograde (positive). The first non-axisymmetric perturbation to bifurcate is the $m=23$ perturbation shown in figure 11 at $Ra=2378.6$, followed by the $m=22$ perturbation at $Ra=2380.02$. The critical Ra is determined from computing the growth rates from time series such as that shown in figure 9(*a*) at a few different Ra bracketing the zero growth rate value and then estimating the critical Ra using linear interpolation to zero growth rate.

Unlike the $Fr=0$ case, when Fr is set to that of the analogous laboratory experiments, a single Fourier mode solution emerging from a supercritical Hopf bifurcation is observed immediately at the onset of three-dimensional convection. For the parameter space explored, an $m=23$ rotating wave was observed; a snapshot of the nonlinear saturated solution is shown in figure 12(*a*). The time series of this evolution (figure 9*a*) shows that the $m=23$ rotating wave fully saturates in about 12 000 viscous times. Very near the Hopf bifurcation, the saturated solution is essentially a superposition of the axisymmetric basic state and a scalar multiple of the $m=23$ eigenmode. Figure 12(*b*) is the axisymmetric $m=0$ component of the nonlinear saturated rotating wave shown in figure 12(*a*), which is essentially the underlying LSC, and figure 12(*c*) is the $m=23$ Fourier component of the rotating wave which essentially has the same structure as the $m=23$ Hopf eigenmode shown in figure 11(*a*).

3.4. *$Fr=$ 0.00882 secondary instabilities*

Near $Ra=2382$, the $m=23$ rotating wave described above loses stability to an $m=6$ Fourier mode perturbation in a supercritical secondary Hopf bifurcation. (This was determined using the direct numerical stability analysis using the $m=23$ rotating wave as the basic state.) Temporal evolution to the nonlinear saturated state results in a pattern with sixfold symmetry near the axis of rotation, giving a mixed-mode modulated rotating wave with $m=23$ and $m=6$.

Increasing Ra slightly from 2382 to 2386, the modulated rotating wave solution exhibits a ratcheting behaviour, similar to that observed by Gorman *et al.* (1996) and analysed by Golubitsky, LeBlanc & Melbourne (2000) in circular flames. A snapshot is shown in figure 13(*a*). All aspects of the dynamics are not the same as in the flame experiment which has $O(2)$ symmetry in azimuth, whereas the

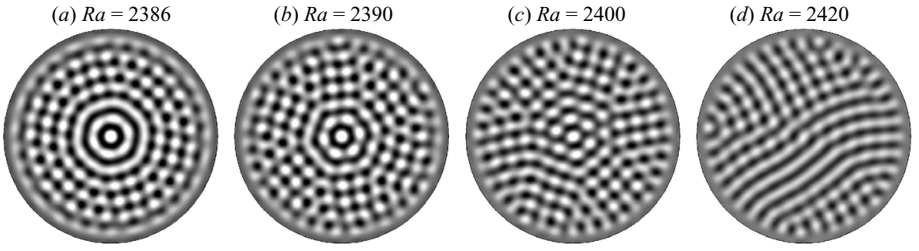

FIGURE 13. Temperature perturbation Θ at $z=0$ for $\Omega=19.7$, $\sigma=4.5$, $\gamma=11.8$, $Fr=8.82\times10^{-3}$ and indicated Ra, with colour levels of $\Theta\in[-5\epsilon, 5\epsilon]$ (black to white).

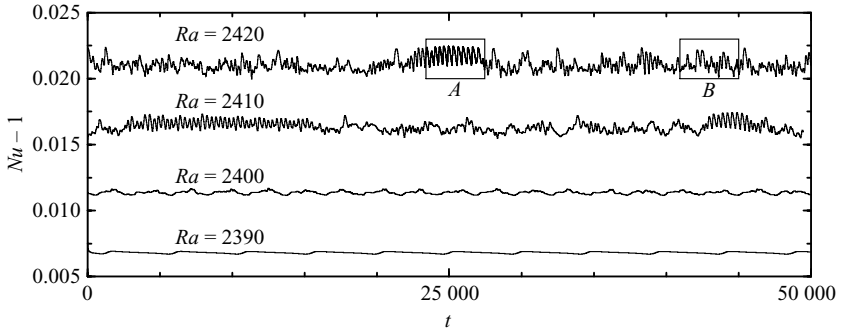

FIGURE 14. Time series of $Nu-1$ at $\Omega=19.7$, $\sigma=4.5$, $\gamma=11.8$, $Fr=8.82\times10^{-3}$ and Ra as indicated.

rotating convection problem only has $SO(2)$ symmetry in azimuth (for discussions of the dynamic consequences of these two symmetries, particularly in the context of hydrodynamic instabilities, see Crawford & Knobloch 1991; Knobloch 1994, 1996), but the ratcheting is very similar. A snapshot of the ratcheting state is shown in figure 13(*b*), but the spatio-temporal nature of this state at $Ra=2390$ is better appreciated from supplementary movie 4.

By $Ra=2400$, roll-switching behaviour is observed on top of the underlying ratcheting lattice found at the slightly lower Ra. A snapshot of one such solution is shown in figure 13(*c*), and supplementary movie 5 illustrates the dynamics. With increasing Ra, the dynamics resemble the Küppers–Lortz-like dynamics described by the experimentalists, where roll-switching domain chaos is observed. A snapshot of a typical solution is shown in figure 13(*d*). However, the time series for this state shows excursions to states exhibiting simpler temporal behaviour, as highlighted in the box labelled A in figure 14 for $Ra=2420$ (supplementary movie 6 shows the temporal evolution of this state over the time indicated by box A). Supplementary movie 7 shows the more typical dynamic behaviour of this flow state over the time marked by box B in figure 14. For comparison, the flow state with all the same parameters, except for $Fr=0$, is shown in supplementary movie 8; it corresponds to time evolution over the period shown by box A in figure 7. At $Ra=2420$, the spatio-temporal characteristics are almost indistinguishable between the $Fr=0$ and the $Fr=8.82\times10^{-3}$ solutions, except that in the $Fr\neq0$ case, the axis $r=0$ remains a distinguished point and the pattern shows intermittent circular organization at the axis.

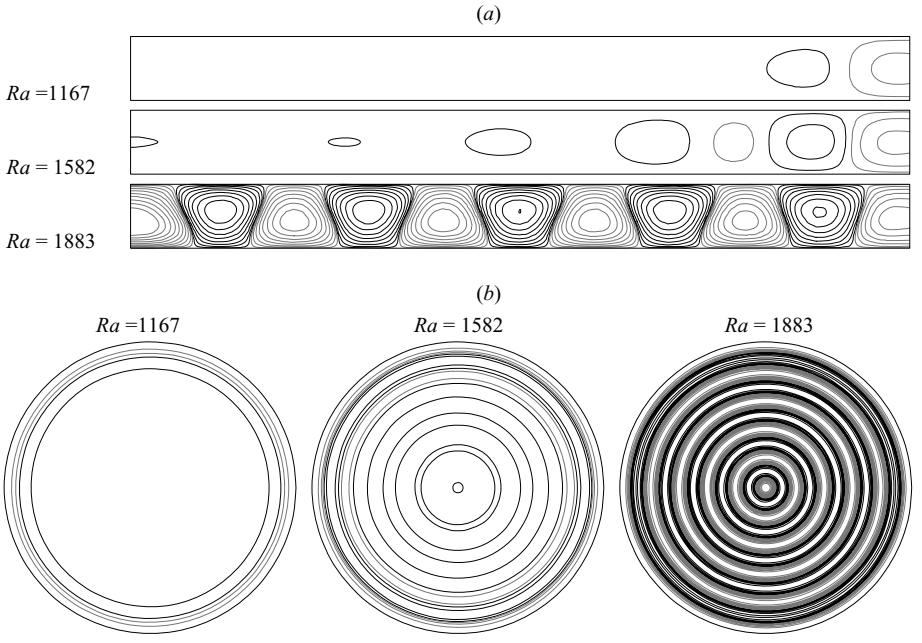

FIGURE 15. Contours of Θ for numerical simulations following Koschmieder (1967) with $\Omega = 1.48$, $\sigma = 877$, $\gamma = 10.3$ and $Fr = 0.025$. (*a*) Meridional planes $r \in [0, \gamma]$, $z \in [-1/2, 1/2]$ of solutions with indicated *Ra*. (*b*) Contours of Θ in a horizontal plane with $z = 0$ for the cases shown in (*a*). Ten positive (black) and negative (grey) contours are spaced quadratically for $\Theta \in [-0.2, 0.2]$.

4. Experimental evidence of the centrifugally driven large scale circulation

So far, our discussion has been focused on parameter regimes of typical laboratory experiments in which the Coriolis force was dominant over the centrifugal force, and we have seen that if the centrifugal force, although small, is not neglected, the LSC smoothly evolves into a target pattern near the onset of gravitational buoyancy-driven convection. Such a development has been described from a series of laboratory experiments reported by Koschmieder (1967) in which the parameter regime was carefully selected so as to have the centrifugal buoyancy dominant over the Coriolis. The patterns he observed are consistent with the axisymmetric flow solutions of Torrest & Hudson (1974) and Daniels (1980), even though the experimental apparatus used for the study had substantial issues in controlling the thermal boundary conditions at the sidewall, which resulted in the stabilization of otherwise-unstable axisymmetric patterns in the non-rotating case. Despite the sidewall issues, the rationale for the emergence of the target patterns being due to the centrifugally driven LSC (Koschmieder 1993) is consistent with the idealized results of Torrest & Hudson (1974) and Daniels (1980). To further explore this, we have conducted a number of simulations in the parameter regime investigated by Koschmieder (1967), with insulating sidewall boundary condition, and have found excellent agreement with his observations. A sample of those simulations is given in figure 15. We have translated his dimensional parameters into our non-dimensional parameters, and the cases in the figure correspond to a moderate Froude number sequence. The parameters are the aspect ratio $\gamma = 10.3$, slow rotation with the Coriolis number $\Omega = 1.48$, a very high Prandtl number $\sigma = 877$ and the Froude number

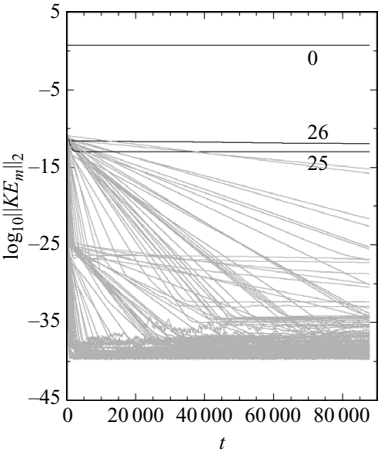

FIGURE 16. Time series of the L2-norm of the kinetic energy associated with each Fourier mode for a simulation with $Ra = 1883$, $\Omega = 1.48$, $\sigma = 877$, $\gamma = 10.3$ and $Fr = 0.025$. The initial condition was an axisymmetric target pattern with a random perturbation of order 10^{-10} across all Fourier modes. The modal energies with $m = 25$ and 26 are shown as black lines, and all other modal energies are shown as grey lines.

$Fr = 0.025$ (about three time larger than that of the results presented in the previous section). The three Ra cases shown in the figure correspond to those in figures 8, 9 and 10 of Koschmieder (1967) and show the same development of the target pattern with increasing Ra and in particular the same number of concentric rolls. We have also conducted a direct numerical linear stability analysis of the $Ra = 1883$ case and found that this solution is stable to three-dimensional perturbations, although perturbations with Fourier modes $m = 25$ and 26 have nearly zero decay rates. The $m = 25$ perturbation is decaying exponentially with a decay constant of -4.2357×10^{-7} per viscous time, and the $m = 26$ case has a decay constant of -4.7873×10^{-6} per viscous time (see figure 16). In a photo of a similar case with $\Omega = 2.96$ and $Fr = 0.1$ in Koschmieder (1967), a high-wavenumber perturbation is evident, much like the $m = 23$ waviness we describe in figure 12(a).

There also provides evidence for the centrifugal buoyancy in the more typical parameter regimes explored experimentally, where the Coriolis dominates over the centrifugal force, but because of the presence of other effects, it has been difficult to unambiguously identify this with the centrifugal buoyancy without detailed simulations. Bajaj *et al.* (2002) reported the intermittent observation of target patterns near the onset, and even beyond the onset where the dynamics are Küppers–Lortz-like, the origin is also intermittently distinguished, much as we observe in supplementary movies 6 and 7, whereas for the same parameters but with $Fr = 0$, supplementary movie 8 does not show any distinguished feature at $r = 0$.

An interesting exercise looking at long-time averages of Küppers–Lortz-type dynamics was conducted by Ning *et al.* (1993), although their intent at the time was not motivated by considerations of the centrifugal buoyancy. In a regime displaying Küppers–Lortz-like dynamics (together with a wall mode), they took very long-time sequences of shadowgraph images and time averaged them. As the flow state is not periodic, very long-time averages were needed, and these converged to a target pattern. This was consistent with what one would expect in a circular container, that the time average should have the same symmetry as the container, but what perhaps was not appreciated at the time was the spatial structure of the time-averaged pattern; it has

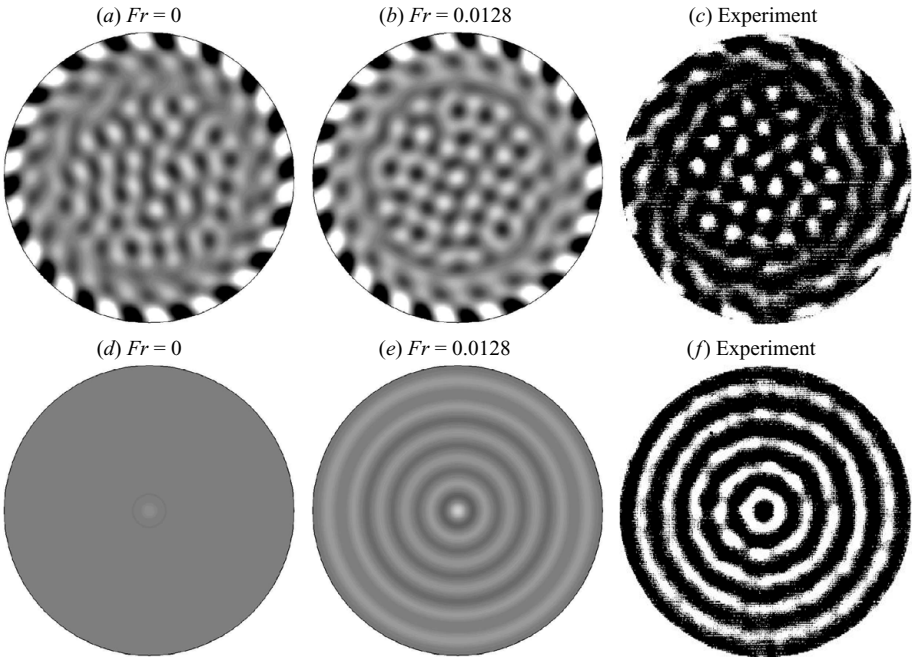

FIGURE 17. Rotating convection in a cylinder with $Ra = 2.08 \times 10^5$ ($\epsilon = 0.053$), $\Omega = 1090$, $\sigma = 6.4$, $\gamma = 2.5$ and $Fr = 0$ or $Fr = 0.0128$; (*a*)–(*c*) are snapshots of a Küppers–Lortz-like state with a precessing wall mode, and (*d*) and (*e*) are the corresponding long-time averages. The experimental results are from Ning *et al.* (1993). A grid resolution of $n_r = 64$, $n_z = 32$ and $n_\theta = 220$ was used in the simulations.

the same structure as the (unstable) axisymmetric LSC at that point in parameter space. To show this, we have computed the same case with the corresponding values of the parameters ($Ra = 2.08 \times 10^5$, $\gamma = 2.5$, $\Omega = 1090$, $\sigma = 6.4$ and $Fr = 0.0128$, where Ra was calculated by considering the given reduced Rayleigh number, $\epsilon = 0.053$, and assuming Ra_c given by Chandrasekhar's estimate for the onset of bulk convection) as well as with $Fr = 0$ and determined the long-time averages of these (taking longer-time averages until they converged). For these calculations $n_r = 64$ and $n_z = 32$ Chebyshev modes were used in r and z, respectively, and $n_\theta = 220$ Fourier modes were used in θ. The results, along with the experimental results are shown in figure 17. It is clear that the $Fr \neq 0$ average is the LSC, and it agrees with the long-time average from the experiment, while the $Fr = 0$ average is the conduction state which is horizontally featureless. So, by taking long-time averages, Ning *et al.* (1993) provided experimental evidence of the centrifugally driven LSC in a Coriolis-dominated parameter regime. We note that the azimuthal wavenumber of the wall mode component of the flow differs between the experiment and our simulation, but this is not surprising, as in the high-Ω regime there is a very large multiplicity of stable states because of a wide Eckhaus–Benjamin–Feir band, and which state is obtained is very sensitive to initial conditions (Lopez *et al.* 2007; Marques & Lopez 2008).

5. Conclusions

A detailed analysis of the onset of Küppers–Lortz dynamics in a finite rotating cylinder has been conducted, and particular attention has been paid to the effect of the centrifugal buoyancy in parameter regimes corresponding to typical experimental

set-ups in which the Coriolis force dominates over the centrifugal force. In order to assess the importance of the centrifugal buoyancy, we have first analysed the Froude number $Fr = 0$ case in which centrifugal effects are neglected and then compared it with small $Fr \neq 0$ solutions corresponding to actual values of the Froude number in laboratory experiments.

In both the $Fr = 0$ and $Fr \neq 0$ cases, the first instability of the base flow is a Hopf bifurcation breaking the azimuthal symmetry with an eigenmode that corresponds to a rotating wave, as predicted by dynamical systems theory. However, in the $Fr = 0$ case, a large packet of eigenvalues bifurcate in a very narrow range of parameters. In terms of a reduced Rayleigh number $\epsilon = (Ra - Ra_c(\Omega))/Ra_c(\Omega)$, the first 10 eigenvalues bifurcate in an ϵ range of 2×10^{-4}, well below the experimental uncertainties in the parameter values. Even more important is the fact that the bifurcated solutions saturate into states consisting of localized square patterns, completely different from the individual structure of the bifurcating eigenmodes. These two facts make analyses based on reduced partial differential equations models or even normal forms/centre manifold reductions inappropriate. The analysis presented here, based on direct numerical simulation of the Navier–Stokes–Boussinesq equations, although costly from a numerical point of view because of the proximity to the bifurcation point and the corresponding extremely long transients, is free from the above-mentioned difficulties of the reduced models. This direct analysis has shed light on the nature of the localized square patterns, previously observed in experiments near the onset as well as in other numerical simulations, that the reduced models are unable to explain. These patterns are associated with a tight packet of several eigenvalues bifurcating almost simultaneously and correspond to saturated states involving significant contributions from all the eigenmodes in the packet. The localized square patterns can be clearly observed in an ϵ range of about 2×10^{-3}, one order of magnitude larger than the interval in which the spectral packet bifurcates. For larger ϵ values, it evolves to more complex patterns which increasingly resemble Küppers–Lortz dynamics as ϵ increases beyond about 8×10^{-3}. This complex scenario at the onset of convection, involving a broadband of eigenmodes, is what transpires when centrifugal buoyancy is ignored by taking $Fr = 0$.

For non-zero Froude numbers, even as small as $Fr \lesssim 0.01$, corresponding to typical experimental values, a completely different transition scenario is observed. The base state is no longer the conductive state but an axisymmetric target pattern. The onset of three-dimensional convection is delayed up to $\epsilon = 2 \times 10^{-3}$, and the spectral gap between the different bifurcating eigenvalues is larger: the distance between the two first bifurcating eigenvalues is now 7×10^{-4}, more than three time the size of the range of the first 10 bifurcating eigenvalues in the $Fr = 0$ case. As a result, the bifurcating eigenmode saturates nonlinearly to a state with the same structure as the eigenmode, and subsequent changes in the nonlinear solutions correspond to secondary bifurcations. Here, the normal form approach is applicable and useful, although its region of validity is narrow. With increasing ϵ, a succession of different complex states emerge, resulting in Küppers–Lortz dynamics for ϵ greater than about 2×10^{-2}.

The main conclusions of this analysis are the following. First, for values of Fr that have usually been considered small enough to neglect centrifugal effects, there are important changes in the dynamics sufficiently close to the bifurcation point when the terms involving Fr are retained in the equations. Second, Küppers–Lortz dynamics do not set in as a direct transition from the base state to spatio-temporal complexity in finite systems. Instead, they are the result of a complex process involving

cascades of bifurcations that take place in a very narrow parameter range. Third, even taking $Fr = 0$, these complex processes do not lend themselves to analysis using reduced partial differential equations models, and direct numerical simulation of the Navier–Stokes–Boussinesq equations cannot be avoided. Incorporating $Fr \neq 0$, in which case reduced models cannot be derived, broadens the spectral gaps between the bifurcating modes and allows for a bifurcation theoretic treatment. In the particular case we examined in detail in this paper, we find that as the Rayleigh number is increased, the axisymmetric LSC smoothly evolves into an axisymmetric target pattern which first becomes unstable at a Hopf bifurcation to an $m = 23$ rotating wave, which on further increasing Ra undergoes a secondary Hopf bifurcation to a modulated rotating wave with wavenumbers $m = 23$ and $m = 6$. The oscillations in this modulated rotating wave become increasingly non-uniform, displaying ratcheting characteristics and evolving towards Küppers–Lortz dynamics with further increases in Ra. So, in some sense, the $Fr \neq 0$ problem fits the familiar transition to temporal chaos following a small number of Hopf bifurcations (Ruelle & Takens 1971) but for a spatio-temporal chaos involving symmetry-breaking Hopf bifurcations.

This work was supported in part by the US National Science Foundation grant DMS-0509594, the Spanish and Catalan government grants FIS2007-61585 and SGR-00024 and the Korean Science and Engineering Foundation WCU grant R32-2009-000-20021-0. Rubio was supported by a Fulbright fellowship at UPC (Barcelona, Spain), whose hospitality is warmly appreciated. Computations were performed using the ASU Fulton High Performance Computing Initiative and the Ranger cluster using the NSF Teragrid grant TG-DMS090029.

Supplementary movies available at journals.cambridge.org/flm.

REFERENCES

Ahlers, G. 2006 Experiments with Rayleigh–Bénard convection. In *Dynamics of Spatio-Temporal Cellular Structures: Henri Bénard Centenary Review* (ed. I. Mutabazi, J. E. Wesfreid & E. Guyon), vol. 207, pp. 67–94. Springer.

Avila, M., Belisle, M. J., Lopez, J. M., Marques, F. & Saric, W. S. 2008 Mode competition in modulated Taylor–Couette flow. *J. Fluid Mech.* **601**, 381–406.

Bajaj, K. M. S., Ahlers, G. & Pesch, W. 2002 Rayleigh–Bénard convection with rotation at small Prandtl numbers. *Phys. Rev.* E **65**, 056309.

Bajaj, K. M. S., Liu, J., Naberhuis, B. & Ahlers, G. 1998 Square patterns in Rayleigh–Bénard convection with rotation about a vertical axis. *Phys. Rev. Lett.* **81**, 806–809.

Barcilon, V. & Pedlosky, J. 1967 On the steady motions produced by a stable stratification in a rapidly rotating fluid. *J. Fluid Mech.* **29**, 673–690.

Barkley, D., Tuckerman, L. S. & Golubitsky, M. 2000 Bifurcation theory for three-dimensional flow in the wake of a circular cylinder. *Phys. Rev.* E **61**, 5247–5252.

Becker, N. & Ahlers, G. 2006*a* Domain chaos puzzle and the calculation of the structure factor and its half-width. *Phys. Rev.* E **73**, 046209.

Becker, N. & Ahlers, G. 2006*b* Local wave director analysis of domain chaos in Rayleigh–Bénard convection. *J. Stat. Mech.* **2006**, P12002.

Becker, N., Scheel, J. D., Cross, M. C. & Ahlers, G. 2006 Effect of the centrifugal force on domain chaos in Rayleigh–Bénard convection. *Phys. Rev.* E **73**, 066309.

Bodenschatz, E., Cannell, D. S., de Bruyn, J. R., Ecke, R., Hu, Y.-C., Lerman, K. & Ahlers, G. 1992 Experiments on three systems with non-variational aspects. *Physica* D **61**, 77–93.

Bodenschatz, E., Pesch, W. & Ahlers, G. 2000 Recent developments in Rayleigh–Bénard convection. *Annu. Rev. Fluid Mech.* **32**, 709–778.

Brummell, N., Hart, J. E. & Lopez, J. M. 2000 On the flow induced by centrifugal buoyancy in a differentially-heated rotating cylinder. *Theoret. Comput. Fluid Dyn.* **14**, 39–54.

Chandrasekhar, S. 1961 *Hydrodynamic and Hydromagnetic Stability*. Oxford University Press.

Cox, S. M. & Matthews, P. C. 2000 Instability of rotating convection. *J. Fluid Mech.* **403**, 153–172.

Crawford, J. D. & Knobloch, E. 1991 Symmetry and symmetry-breaking bifurcations in fluid dynamics. *Annu. Rev. Fluid Mech.* **23**, 341–387.

Cross, M. C., Meiron, D. & Tu, Y. 1994 Chaotic domains: a numerical investigation. *Chaos* **4**, 607–619.

Daniels, P. G. 1980 The effect of centrifugal acceleration on axisymmetric convection in a shallow rotating cylinder or annulus. *J. Fluid Mech.* **99**, 65–84.

Fantz, M., Friedrich, R., Bestehorn, M. & Haken, H. 1992 Pattern formation in rotating Bénard convection. *Physica* D **61**, 147–154.

Fornberg, B. 1998 *A Practical Guide to Pseudospectral Methods*. Cambridge University Press.

Goldstein, H. F., Knobloch, E., Mercader, I. & Net, M. 1993 Convection in a rotating cylinder. Part 1. Linear theory for moderate Prandtl numbers. *J. Fluid Mech.* **248**, 583–604.

Golubitsky, M., LeBlanc, V. G. & Melbourne, I. 2000 Hopf bifurcation from rotating waves and patterns in physical space. *J. Nonlin. Sci.* **10**, 69–101.

Gorman, M., el Hamdi, M., Pearson, B. & Robbins, K. A. 1996 Ratcheting motion of concentric rings in cellular flames. *Phys. Rev. Lett.* **76**, 228–231.

Hart, J. E. 2000 On the influence of centrifugal buoyancy on rotating convection. *J. Fluid Mech.* **403**, 133–151.

Heikes, K. E. & Busse, F. H. 1980*a* Convection in a rotating layer: a simple case of turbulence. *Science* **208**, 173–175.

Heikes, K. E. & Busse, F. H. 1980*b* Weakly nonlinear turbulence in a rotating convection layer. *Ann. NY Acad. Sci.* **357**, 28–36.

Homsy, G. M. & Hudson, J. L. 1969 Centrifugally driven thermal convection in a rotating cylinder. *J. Fluid Mech.* **35**, 33–52.

Homsy, G. M. & Hudson, J. L. 1971 Centrifugal convection and its effect on the asymptotic stability of a bounded rotating fluid heated from below. *J. Fluid Mech.* **48**, 605–624.

Hu, Y., Ecke, R. E. & Ahlers, G. 1997 Convection under rotation for Prandtl numbers near 1: linear stability, wavenumber selection, and pattern dynamics. *Phys. Rev.* E **55**, 6928–6949.

Hu, Y., Pesch, W., Ahlers, G. & Ecke, R. E. 1998 Convection under rotation for Prandtl numbers near 1: Küppers–Lortz instability. *Phys. Rev.* E **58**, 5821–5833.

Hughes, S. & Randriamampianina, A. 1998 An improved projection scheme applied to pseudospectral methods for the incompressible Navier–Stokes equations. *Intl J. Numer. Meth. Fluids* **28**, 501–521.

Jayaraman, A., Scheel, J. D., Greenside, H. S. & Fisher, P. F. 2006 Characterization of the domain chaos convection state by the largest Lyapunov exponent. *Phys. Rev.* E **74**, 016209.

Knobloch, E. 1994 Bifurcations in rotating systems. In *Lectures on Solar and Planetary Dynamos* (ed. M. R. E. Proctor & A. D. Gilbert), pp. 331–372. Cambridge University Press.

Knobloch, E. 1996 Symmetry and instability in rotating hydrodynamic and magnetohydrodynamic flows. *Phys. Fluids* **8**, 1446–1454.

Knobloch, E. 1998 Rotating convection: recent developments. *Intl J. Engng Sci.* **36**, 1421–1450.

Koschmieder, E. L. 1967 On convection on a uniformly heated rotating plane. *Beitr. Phys. Atmos.* **40**, 216–225.

Koschmieder, E. L. 1993 *Bénard Cells and Taylor Vortices*. Cambridge University Press.

Küppers, G. 1970 The stability of steady finite amplitude convection in a rotating fluid layer. *Phys. Lett.* A **32**, 7–8.

Küppers, G. & Lortz, D. 1969 Transition from laminar convection to thermal turbulence in a rotating fluid layer. *J. Fluid Mech.* **35**, 609–620.

Lewis, G. M. & Nagata, W. 2003 Double Hopf bifurcations in the differentially heated rotating annulus. *SIAM J. Appl. Math.* **63**, 1029–1055.

Lopez, J. M., Cui, Y. D. & Lim, T. T. 2006*a* An experimental and numerical investigation of the competition between axisymmetric time-periodic modes in an enclosed swirling flow. *Phys. Fluids* **18**, 104106.

Lopez, J. M. & Marques, F. 2009 Centrifugal effects in rotating convection: nonlinear dynamics. *J. Fluid Mech.* **628**, 269–297.

Lopez, J. M., Marques, F., Mercader, I. & Batiste, O. 2007 Onset of convection in a moderate aspect-ratio rotating cylinder: Eckhaus–Benjamin–Feir instability. *J. Fluid Mech.* **590**, 187–208.

Lopez, J. M., Rubio, A. & Marques, F. 2006*b* travelling circular waves in axisymmetric rotating convection. *J. Fluid Mech.* **569**, 331–348.

Marques, F., Gelfgat, A. Y. & Lopez, J. M. 2003 A tangent double Hopf bifurcation in a differentially rotating cylinder flow. *Phys. Rev.* E **68**, 016310.

Marques, F. & Lopez, J. M. 2008 Influence of wall modes on the onset of bulk convection in a rotating cylinder. *Phys. Fluids* **20**, 024109.

Marques, F., Lopez, J. M. & Shen, J. 2002 Mode interactions in an enclosed swirling flow: a double Hopf bifurcation between azimuthal wavenumbers 0 and 2. *J. Fluid Mech.* **455**, 263–281.

Marques, F., Mercader, I., Batiste, O. & Lopez, J. M. 2007 Centrifugal effects in rotating convection: axisymmetric states and three-dimensional instabilities. *J. Fluid Mech.* **580**, 303–318.

Mercader, I., Net, M. & Falqués, A. 1991 Spectral methods for high order equations. *Comp. Meth. Appl. Mech. Engng* **91**, 1245–1251.

Niemela, J. J. & Donnelly, R. J. 1986 Direct transition to turbulence in rotating Bénard convection. *Phys. Rev. Lett.* **57**, 2524–2527.

Ning, L., Hu, Y., Ecke, R. & Ahlers, G. 1993 Spatial and temporal averages in chaotic patterns. *Phys. Rev. Lett.* **71**, 2216–2219.

Orszag, S. A. & Patera, A. T. 1983 Secondary instability of wall-bounded shear flows. *J. Fluid Mech.* **128**, 347–385.

Ponty, Y., Passot, T. & Sulem, P. L. 1997 Pattern dynamics in rotating convection at finite Prandtl number. *Phys. Rev.* E **56**, 4162–4178.

Rodríguez, J. M., Pérez-García, C., Bestehorn, M., Fantz, M. & Friedrich, R. 1992 Pattern formation in convection of rotating fluids with broken vertical symmetry. *Phys. Rev.* A **46**, 4729–4735.

Rossby, H. T. 1969 A study of Bénard convection with and without rotation. *J. Fluid Mech.* **36**, 309–335.

Rubio, A., Lopez, J. M. & Marques, F. 2008 Modulated rotating convection: radially travelling concentric rolls. *J. Fluid Mech.* **608**, 357–378.

Rubio, A., Lopez, J. M. & Marques, F. 2009 Interacting oscillatory boundary layers and wall modes in modulated rotating convection. *J. Fluid Mech.* **625**, 75–96.

Ruelle, D. & Takens, F. 1971 On the nature of turbulence. *Comm. Math. Phys.* **20**, 167.

Sánchez-Álvarez, J. J., Serre, E., Crespo del Arco, E. & Busse, F. H. 2005 Square patterns in rotating Rayleigh–Bénard convection. *Phys. Rev.* E **72**, 036307.

Scheel, J. D. 2007 The amplitude equation for rotating Rayleigh–Bénard convection. *Phys. Fluids* **19**, 104105.

Thompson, K. L., Bajaj, K. M. S. & Ahlers, G. 2002 travelling concentric-roll patterns in Rayleigh-Bénard convection with modulated rotation. *Phys. Rev.* E **65**, 04618.

Torrest, M. A. & Hudson, J. L. 1974 The effect of centrifugal convection on the stability of a rotating fluid heated from below. *Appl. Sci. Res.* **29**, 273–289.

Tu, Y. & Cross, M. C. 1992 Chaotic domain structure in rotating convection. *Phys. Rev. Lett.* **69**, 2515–2518.

Zhong, F., Ecke, R. & Steinberg, V. 1991 Asymmetric modes and the transition to vortex structures in rotating Rayleigh–Bénard convection. *Phys. Rev. Lett.* **67**, 2473–2476.